OPEN ACCESS

Modelling Water Transport Limitations and Ionic Voltage Losses in Bipolar Membrane Water Electrolysis

To cite this article: Oskar Weiland *et al* 2023 *J. Electrochem. Soc.* **170** 054505

Journal of The Electrochemical Society, 2023 **170** 054505

Modelling Water Transport Limitations and Ionic Voltage Losses in Bipolar Membrane Water Electrolysis

Oskar Weiland, Patrick Trinke,[z] Boris Bensmann, and Richard Hanke-Rauschenbach

Electrical Energy Storage Systems, Leibniz Universität Hannover, 30167 Hannover, Germany

This work analyses the water transport and ionic losses in bipolar membranes at water electrolysis cells conditions. In common bipolar setups, water is split at the bipolar interface between the anion exchange membrane (AEM) and the cation exchange membrane (CEM). Accordingly, ions (protons and hydroxide ions) are transported to the electrodes, carrying the water out of both membranes via electro-osmotic drag. These outfluxes plus the required water amount for the splitting process have to be compensated by water diffusion towards the bipolar interface. The effect of water transport on the polarisation behaviour is additionally shown. Mayerhöfer et al. [*ACS Appl. Energy Mater.*, **3**, 9635 (2020)] and Oener et al.[*ACS Energy Lett.*, **6**, 1 (2021)] decreased polarization losses and increased the current density range by reducing either the AEM or the CEM thickness, respectively. Our model validates these improvements by calculating the limiting current density caused by dehydration of the membranes. Further analysis shows that thinner AEM thicknesses decrease membrane voltage losses more than thinner CEM due to lower ionic conductivities and faster dehydration of AEMs. Thin CEMs on the other hand, are more efficient at increasing the limiting current density.

 [DOI: 10.1149/1945-7111/acd02c]

Manuscript submitted December 2, 2022; revised manuscript received April 3, 2023. Published May 17, 2023.

Focus of this study is a model-based investigation of water transport in Bipolar Membrane Water Electrolysis (BPMWE). Research interest in BPMWE for hydrogen production has increased recently. Firstly, it is possible to omit the expensive and rare iridium catalyst on the anode, which is widely used in Cation Exchange Membrane (CEM) electrolyzers. Secondly, expensive titanium can be replaced for the bipolar plate and porous transport layer in BPMWE because of a less corrosive alkaline environment at the anode.[1]

For both fuel cell and electrolysis mode with BPMs, two theoretical configurations are possible, as it can be seen in Fig. 1. The water splitting (WS) electrolysis in quadrant 1 is discussed here. Kinetics for the oxygen evolution reaction are favorable in alkaline environments whereas hydrogen evolution reactions are favorable in acidic environments.[2,3]

Experimental studies of BPMWE mostly demonstrated low current density operation.[1,4,5] Only by significantly reducing the thickness of either the AEM or the CEM within the sandwich higher current densities could be achieved. Mayerhöfer et al.[6] reduced the AEM thickness to 3 μm (CEM thickness remained at 51 μm) and measured current densities up to 1.7 A cm^{-2}. Even higher current densities are reported by Oener et al.[7] for a thin CEM (2 μm, with AEM of 50 μm) up to 4 A cm^{-2}. Furthermore, both groups reported significant lower cell voltages.

A model focusing on the electrochemical processes was presented by Wrubel et al.[9] The results covered low current density operation. Zhang et al.[10] similarly presented a model, which was evaluated for low current densities with a focus on polarization. Bui et al.[11] developed an ion transport model optimized for a longer electrolyzer lifespan. In all available studies, only little attention has been paid to the water management inside the BPM and a fundamental explanation for the improvements with thin membranes is still missing.

The objective of the present paper is a model-based explanation for the improvements with thin membranes in BPMWE. A water transport model is introduced for this purpose. In addition, a simple electrochemical model covers the polarization behavior of the cell. The results divide into three parts: First, model results are shown for operation with equally thick AEM and CEM. Second, the experimental performance improvements of the literature with one thin membrane are explained. Third, a wider membrane thickness variation for AEM and CEM thickness is performed.

Model

The model presented here includes two separate sub-models: (i) a one-dimensional through-plane water transport model within the BPM, and (ii) a simple 0D electrochemical performance model that also accounts the local ionic voltages losses for 1D ionic membrane conductivities depending on membrane water content.

Water transport model.—Figure 2 displays the schematic structure of the water transport model. AEM and CEM face each other in the middle at the bipolar interface (BPI). The variables j and k discretize the AEM and CEM in the through-plane coordinate. Liquid water feeds on both sides is assumed and thus that liquid water is present at the outer BPM boundaries.

The relationship between water content and concentration is defined in Eq. 1 according to Weber and Newman.[12]

$$\lambda = \frac{\frac{EW}{\rho^{\mathrm{dry}}}}{\frac{1}{c} - \frac{M_{\mathrm{H_2O}}}{\rho_l}} \qquad [1]$$

Here, EW is the equivalent membrane weight of membrane, and ρ^{dry} denotes the dry membrane density for the AEM and CEM material, respectively. Values for EW and ρ^{dry} are taken from Peng et al.[13] Increasing water content linearly increases the membrane volume as it can be seen on the right side of Eq. 1. There, $M_{\mathrm{H_2O}}$ denotes the molar water weight and the ρ_l the liquid water density. For better understanding, water content is depicted instead of water concentration.

Water content gradients between the volumes are the driving force for diffusional water fluxes. Since water flux towards the BPI benefits the WS reaction at the BPI, fluxes are defined positively in the direction to the BPI. Therefore, the drag flux directions are defined as opposite to their expected physical flux direction, as H^+ cations and OH^- anions migrate from the BPI to the outer boundaries and drag water from the BPI to the outer BPM boundaries.

[z]E-mail: patrick.trinke@ifes.uni-hannover.de

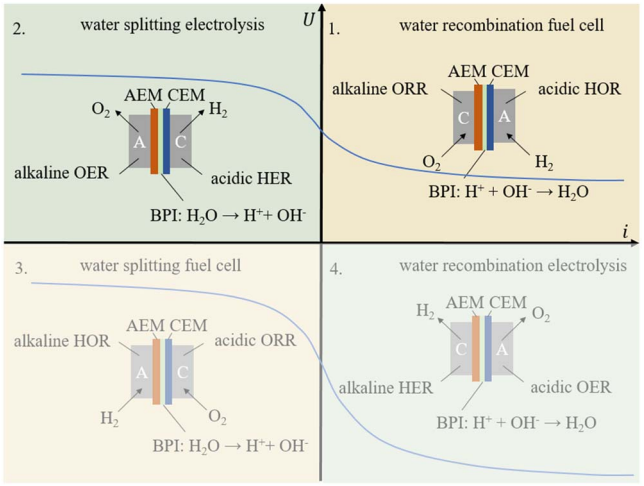

Figure 1. Possible fuel cell and electrolysis modes with BPMs: Water can recombine or split at the BPI depending on the operation. The top construction with an acidic hydrogen and alkaline oxygen side is favorable for application because of favourable reaction kinetics for both fuel cell (quadrant 1) and electrolysis (quadrant 2), whereas the bottom two configurations are technically not relevant.[8] The reaction equations for all possible configurations are listed in the Appendix (Table A-I).

Steady-state water balance conditions are assumed, as shown in Eq. 2.

$$0 = \frac{\mathrm{d}c}{\mathrm{d}t} = \frac{\mathrm{d}}{\mathrm{d}x}(N^{\mathrm{diff}} + N^{\mathrm{drag}}) \qquad [2]$$

Diffusional flux N^{diff} and electro-osmotic drag N^{drag} are linearly superimposed.

Fick's law is used here in Eq. 3 with concentration gradients driving the diffusional water flux and the electro-osmotic dragged water flux is calculated of Eq. 4. For consistency, the electro-osmotic drag is defined opposite of the physical flux, whereas the diffusion flux is defined positively to the physical flux, so that both fluxes are defined positively into the BPI.

$$N^{\mathrm{diff}}_{\mathrm{AEM}} = -D^{\mathrm{AEM}}(\lambda_{\mathrm{AEM}})\frac{dc}{dx} \qquad [3]$$

$$N^{\mathrm{diff}}_{\mathrm{CEM}} = D^{\mathrm{CEM}}(\lambda_{\mathrm{CEM}})\frac{dc}{dx} \qquad [4]$$

$$N^{\mathrm{drag}}_{\mathrm{AEM/CEM}} = -n^{\mathrm{drag,AEM/CEM}}(\lambda_{\mathrm{AEM/CEM}})\frac{i_{\mathrm{OH^-/H^+}}}{\mathrm{F}} \qquad [5]$$

A

Diffusion coefficients $D^{\mathrm{AEM/CEM}}(\lambda_{\mathrm{AEM/CEM}})$ for the AEM and CEM depend on the water content as well as the drag coefficient n^{drag}. The relationships for the diffusion coefficients $D^{\mathrm{AEM/CEM}}$ and drag coefficients $n^{\mathrm{drag,AEM/CEM}}$ are listed in the Appendix. Both differ in alkaline and acidic media and thus in AEM and CEM.

Second order boundary conditions take effect in two regions, at the BPI and at the outer BPM boundaries. At the BPI, the water balance (Eq. 6) takes into account the water consumption (Eq. 6) σ_{BPI} due to the water splitting reaction.

$$0 = N^{\mathrm{diff}}_{\mathrm{AEM},1} + N^{\mathrm{diff}}_{\mathrm{CEM},1} + N^{\mathrm{drag}}_{\mathrm{AEM},1} + N^{\mathrm{drag}}_{\mathrm{CEM},1} - \sigma_{\mathrm{BPI}} \qquad [6]$$

$$\sigma_{\mathrm{BPI}} = \frac{i}{2\mathrm{F}} \qquad [7]$$

The activity of anions and cations are assumed constantly throughout the membrane because of the stationary end groups (Eqs. 8, 9).

$$a^{\mathrm{BC}}_{\mathrm{H^+}} = a^{\mathrm{BPI}}_{\mathrm{H^+}} = const. \qquad [8]$$

$$a^{\mathrm{BC}}_{\mathrm{OH^-}} = a^{\mathrm{BPI}}_{\mathrm{OH^-}} = const. \qquad [9]$$

The water activity, changes within the membrane. However, at the BPI, the water activity of the AEM-equivalent and CEM-

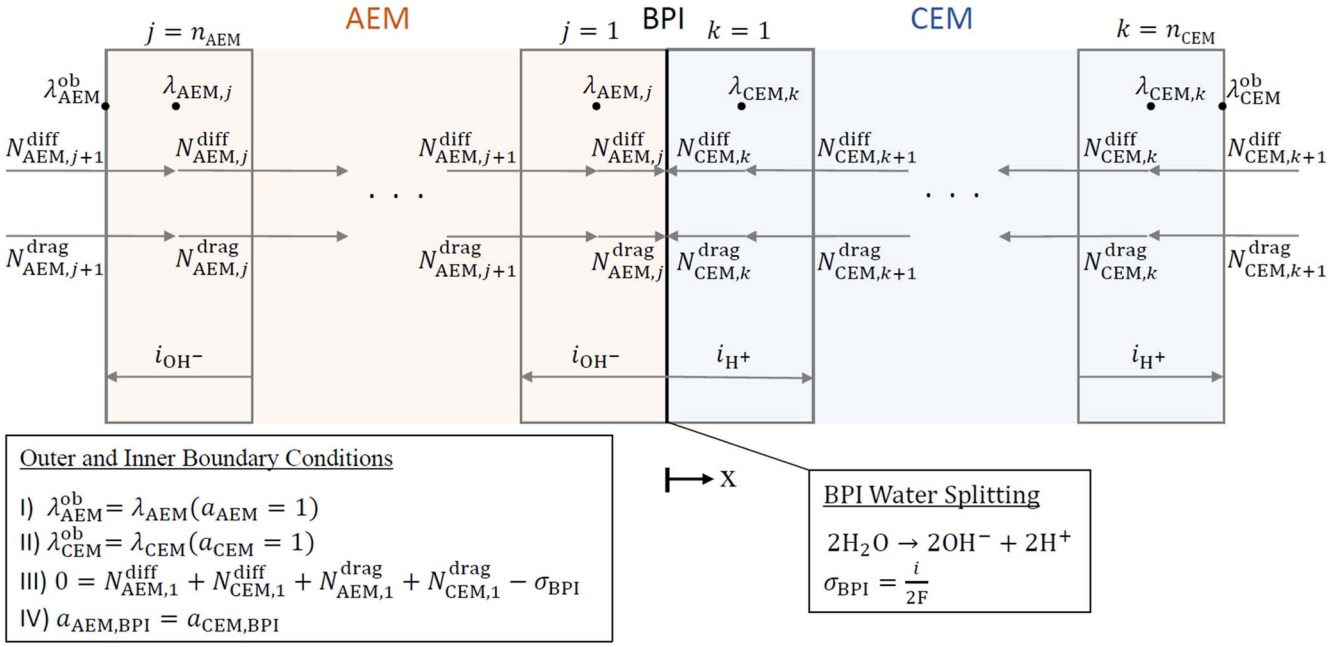

Figure 2. Structure of water transport model with AEM on the left, CEM on the right, and the BPI in between. Reaction equation, sink term, and the boundary conditions (I)–(IV) are given in the boxes below, with (I) and (II) saturation at the outer membrane boundaries, (III) water balance at the BPI and IV) equal AEM and CEM activity at the BPI. Note that water content is chosen for the figures, while the model calculation uses water concentration. The directions of diffusion fluxes are defined positively in their physical direction into the BPI whereas the drag fluxes are defined positively into the BPI and opposite to the physical flux. This is made because a positive flux into the BPI enables the water splitting reaction.

equivalent are assumed equal (Eq. 10).

$$a_{\mathrm{AEM,BPI}} = a_{\mathrm{CEM,BPI}} \quad [10]$$

Since liquid water floods the outer BPM boundaries water content is calculated with unity water activity for AEM $\lambda^{\mathrm{ob}}_{\mathrm{AEM}}(a_{\mathrm{AEM}} = 1)$ and CEM $\lambda^{\mathrm{ob}}_{\mathrm{CEM}}(a_{\mathrm{CEM}} = 1)$.

The relationships of λ and the activity a are presented in the Appendix.

Electrochemical model.—A simple galvanostatic model with uniform ion flux (Eq. 11) is utilized to demonstrate the electrical cell behavior. The ion flux is

$$i_{\mathrm{OH^-}} = i_{\mathrm{H^+}} = i \quad [11]$$

The cell voltage U_{cell} in Eq. 12 considers activation overpotentials at the electrodes and the BPM as well as ionic voltage losses inside the AEM and CEM.

$$U_{\mathrm{cell}} = U_{\mathrm{rev}} + \eta_{\mathrm{a}} + |\eta_{\mathrm{c}}| + \eta_{\mathrm{ws}} + \Delta U_{\mathrm{AEM}} + \Delta U_{\mathrm{CEM}} \quad [12]$$

The reversible cell voltage U_{rev} is calculated in Eq. 13 under assumed isobar ($p_{\mathrm{cell}} = 1$ bar) and isothermal conditions ($T_{\mathrm{cell}} = 80$ °C)[14]

$$U_{\mathrm{rev}} = 1.1795\ \mathrm{V} \quad [13]$$

Ohmic voltage losses need to be considered locally in Eq. 14. This is due to the possible partly dehydration of the BPM and the water dependent ionic conductivities within the BPM.

$$\Delta U_{\mathrm{AEM},j/\mathrm{CEM},k} = i \cdot \frac{\delta_{j/k}}{\sigma_{\mathrm{AEM},j/\mathrm{CEM},k}} \quad [14]$$

The conductivities approaches $\sigma_{\mathrm{AEM},j/\mathrm{CEM},k} = f(\lambda)$ can be found in the SI. Summing up the losses of every j and k yields the overall ohmic losses of the AEM (Eq. 15) and CEM (Eq. 16), respectively.

$$\Delta U_{\mathrm{AEM}} = \sum \Delta U_{\mathrm{AEM},j} \quad [15]$$

$$\Delta U_{\mathrm{CEM}} = \sum \Delta U_{\mathrm{CEM},k} \quad [16]$$

In the reaction zones, the anodic activation overpotential η_{a}, the cathodic activation overpotential η_{c}, and the BPI water splitting overpotential η_{ws} increase the cell voltage.

Tafel kinetics are used both for anodic and cathodic activation overpotential.[15] The anodic activation overpotential in Eq. 17 in the BPMWE correspond to those of AEM electrolysis,

$$\eta_{\mathrm{a}} = \beta^{\mathrm{a}} \cdot \ln\left(\frac{i}{i_{0,\mathrm{a}}}\right) \quad [17]$$

with $\beta^{\mathrm{a}} = 0.0189$ V/dec at 80 °C and $i_{0,a} = 0.37$ A/m^2.[16,17] At the cathode, a CEMWE-similar reaction exists (Eq. 18).[15]

$$|\eta_{\mathrm{c}}| = \beta^{\mathrm{c}} \cdot \ln\left(\frac{i}{i_{0,\mathrm{c}}}\right) \quad [18]$$

Here, β_{c} is 0.0304 V dec^{-1} and $i_{0,\mathrm{c}}$ is 400 A m^{-2} at 80 °C.[18]

Whether the reaction at the BPI should be modelled with the depletion layer theory or the neutral layer theory is currently subject of scientific debate.[19] Without taking a position in this debate, the Butler-Vollmer approach of Peng et al.[18] originated from Hurwitz et al.[20] is used here to account for voltage losses at the BPI (Eq. 19).

$$i = i_{0,\mathrm{ws}}\left(\exp\left(\frac{\alpha_{\mathrm{ws}} \mathrm{F} \eta_{\mathrm{ws}}}{\mathrm{R}T}\right) - \exp\left(-\frac{(1-\alpha_{\mathrm{ws}})\mathrm{F}\eta_{\mathrm{ws}}}{\mathrm{R}T}\right)\right) \quad [19]$$

Additional information about this approach is listed in the Appendix.

Results

For a general understanding of water transport limitations in BPMWE, the model is first evaluated at a fixed current density and base case membrane thicknesses of $\delta_{\mathrm{AEM}} = 80\ \mu$m and $\delta_{\mathrm{CEM}} = 80\ \mu$m. After these fixed current density results, findings for operation under different current densities are shown. Subsequently, model results with specifically reduced membrane thicknesses of either AEM or CEM explain the previously obtained improvements in the literature of Mayerhöfer et al.[6] and Oener et al.[7] The results section closes with findings for variable AEM and CEM thicknesses.

Fixed current density.—Fixing the current density at $i = 0.5$ A/cm^2 yields the BPM water content shown in Fig. 3a. Low water content appears close to the BPI in both AEM and CEM. As the outer boundaries are saturated with liquid water, the highest water content is found there. A nonlinear decrease is found in between.

Reasons for this curve are water diffusion and electro-osmotic drag curves as well as the BPI consumption due to the reaction as shown in Fig. 3b. Generally, diffusional flux inside the CEM is higher than in the AEM, while more water is dragged through the AEM. Under these conditions, the total water transport to the BPI is negative through the AEM and positive through the CEM.

As the ionic conductivities of the membranes depend on water content, the curve of Fig. 2a directly determines the BPM conductivity in Fig. 4a. The highest overall ionic conductivities exist close to the outer BPM boundaries, whereas the highest local ionic voltage losses are close to the BPI where the water content is the lowest. The CEM is in general more conductive for H^+ ions than the AEM for OH^-. Using equally thick membranes therefore result in a higher ionic voltage loss from the AEM, as shown in Fig. 4b.

Variable current density.—Water content inside the BPM depends harshly on the applied current density, as it is shown in Fig. 5a. With increasing current densities, more water is consumed at the BPI and dragged towards the outer BPM boundaries. The corresponding reduction of the BPMs water content triggers water diffusion towards the BPI. The properties of the membranes regarding water diffusion define the intensity of the diffusion flux. The AEM reacts more harshly than the CEM. Above 1 A cm^{-2}, a water content plateau of a uniform λ arises inside the AEM from the BPI. Inside this plateau, a missing water content gradient hinders diffusive water flux from the AEM to the BPI. As a result, electro-osmotic drag by the OH^- ions is the one-way water transport mechanism. Because of this dehydration inside the BPM, the cell cannot be operated above the limiting current density. At this limiting current density of 1.56 A cm^{-2}, the diffusive water transport through the CEM fails to feed the reaction and the negative drag fluxes.

In Fig. 5b the water transport mechanisms into the BPI and the BPI consumption of the reaction are shown. Adding up diffusive and drag-driven flux yields the total flux for each membrane. In the CEM, diffusion dominates water transport over the operating range while drag dominates AEM transport mechanisms. Due to the high drag flux, the AEM removes more water from the BPI than the water splitting reaction at low current densities. At (I), AEM diffusion into the BPI collapses already below 0.5 A cm^{-2}. Reason is the decreasing water content of the AEM (a) as well as the diffusion and drag coefficient dependencies. Therefore, CEM diffusion mainly

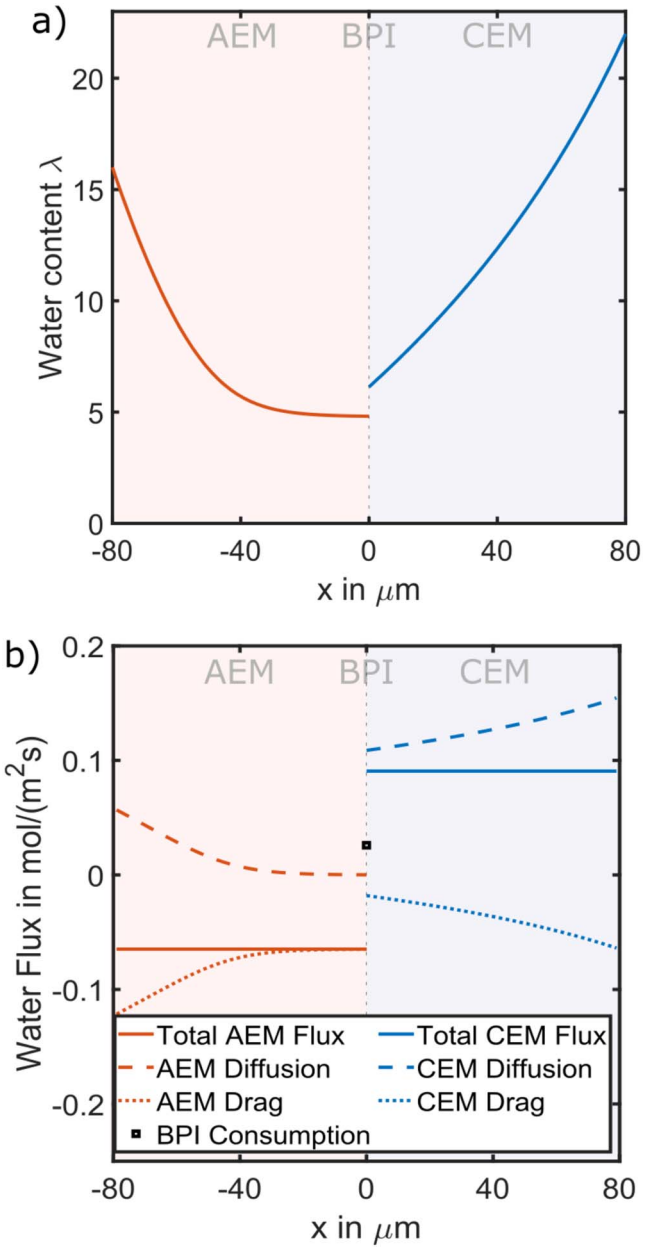

Figure 3. (a) Water Content inside the BPM. (b) Water fluxes inside the BPM, high diffusion through CEM and high electro-osmotic drag through AEM. Conditions: p = 1 bar, T = 80 °C and i = 0.5 A cm^{-2}.

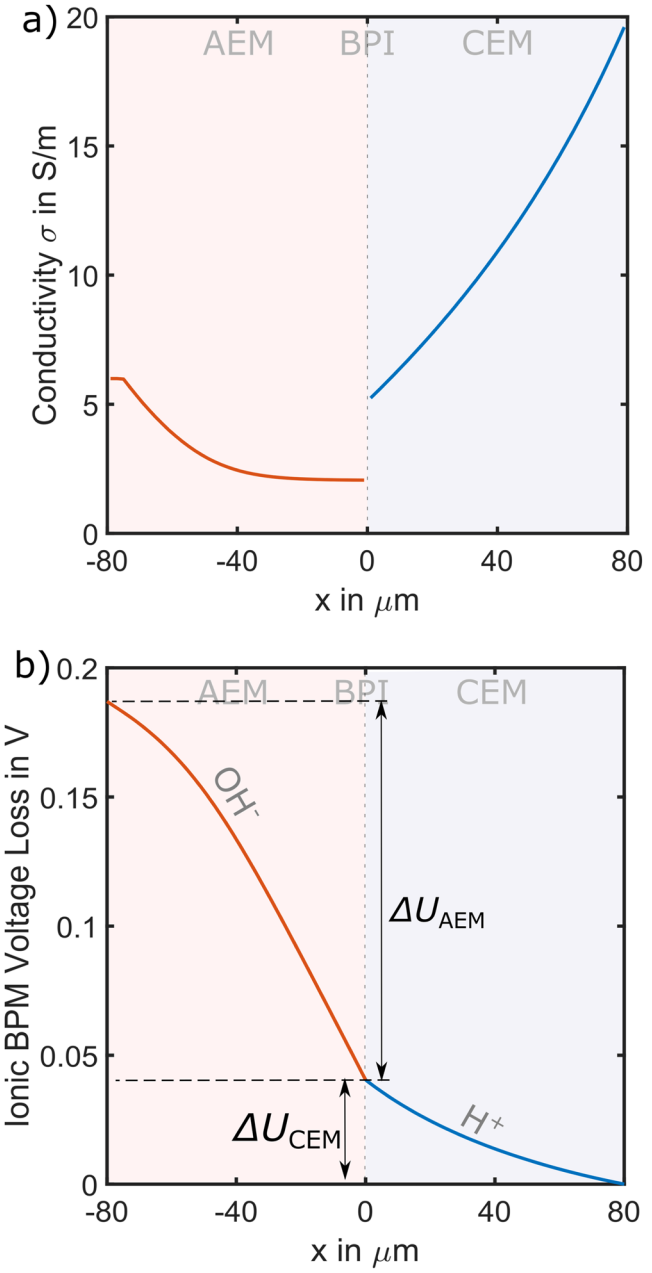

Figure 4. (a) Ionic conductivity decreases at low water content and increases in CEM. (b) Lower AEM conductivity leads to higher voltage losses on AEM side of BPM. Conditions: p = 1 bar, T = 80 °C and i = 0.5 A cm^{-2}.

feeds both drag fluxes and the water splitting reaction. It remains as the only water feeding flux. At a current density of 0.79 A cm^{-2}, CEM diffusion flux has its maximum (II). This maximum results from smaller diffusion transport coefficients at lower water content. The same mechanism holds for AEM and CEM drag flux maxima. These relations cause the opposing effect of decreasing diffusion and decreasing drag at the same time, which offset each other up to the limiting current density. Up to the limiting current density, CEM diffusion remains as the only water transport mechanism. Due to the absence of water, no drag fluxes can flow in both membranes and due to the absence of a water content gradient, no diffusional transport occurs from the AEM to the BPI. The diffusional transport through the CEM does not cover the demand by drag and BPI consumption and the limiting current density is reached in (III).

In Fig. 5c, a closer look is made to the BPI water content, which can be extracted from Fig. 5a by plotting the AEM- and CEM-equivalent water content points versus the current density. A concave decrease of water content exists in both membranes. At low current densities, the water content already decreases relatively quick, which negatively affects the ionic membrane conductivities.

Considering the effects of dehydration on the migration of ions, the breakdown of membrane voltage losses is shown in Fig. 6a. The ionic voltage losses follow the shape of a concave increase for both AEM and CEM. Lower AEM- than CEM-conductivity leads to the higher absolute ionic losses of the AEM. As the decreases in water content are higher for the AEM (cf. Fig. 4a), due to lower water diffusion coefficients and higher drag coefficients of the AEM material, losses within the AEM increase stronger at increasing current densities.

With an increasing current density, the growing increase of the ionic losses are also reflected in the cell voltage, as shown in Fig. 6b. The grey region represents the impact of the total ionic losses

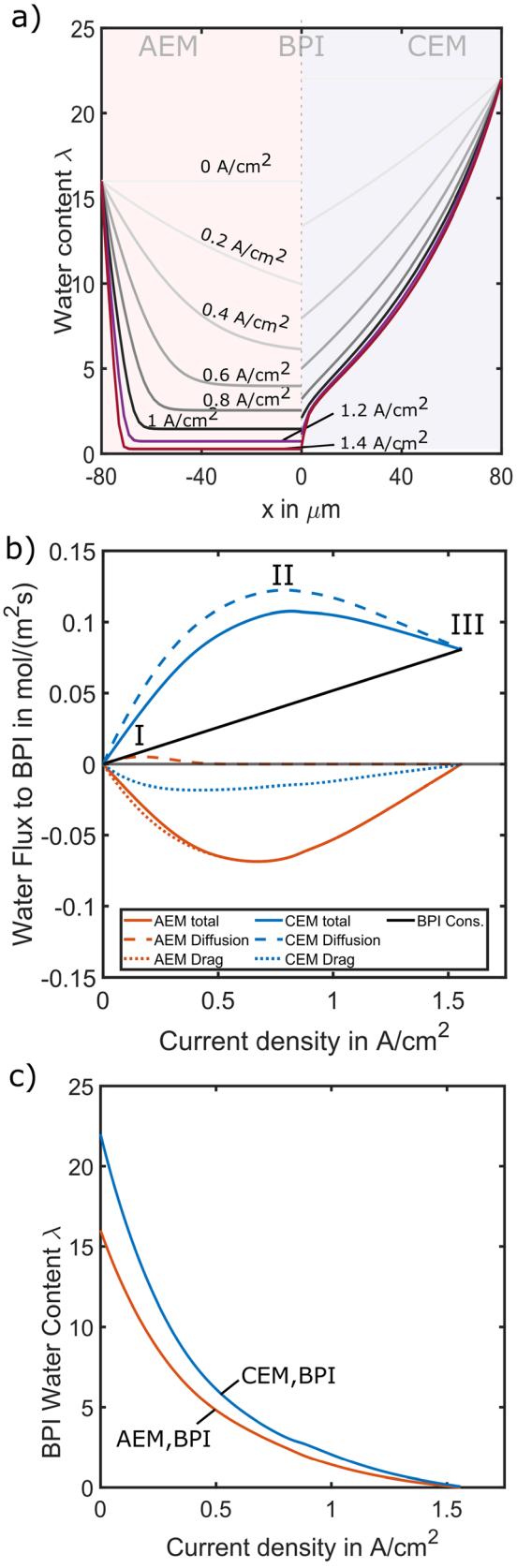

Figure 5. (a) Water content decreases in CEM and especially in AEM at higher current densities. (b) Drag + Diffusion over current density. I: Low AEM diffusion to BPI. II: Peak of CEM diffusion due to decreasing water content. III: Limiting current density. (c) BPI water content decreases comparably in AEM and CEM until limiting current density is reached. Operating conditions: p = 1 bar and T = 80 °C.

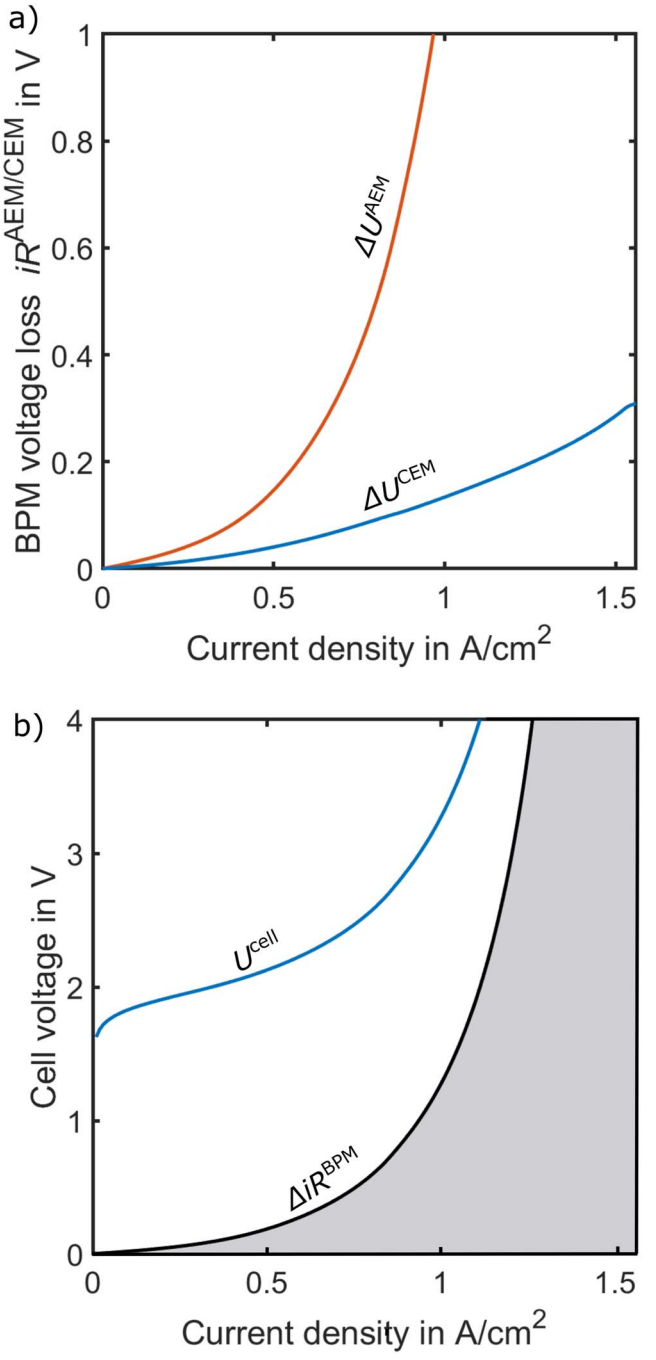

Figure 6. (a) Lower ionic conductivity of the AEM in combination with lower water content leads to higher voltage losses for the AEM compared to the CEM side. (b) The total ionic losses ΔU^{BPM} that originate from the insufficient water transport are the main reasons of the increasing cell voltage. Especially at higher current densities, close to the limiting current density, the drastic effect can be seen. Conditions: p = 1 bar, T = 80 °C.

highlighting the impact on the cell voltage. The polarisation curve can be divided into three regions: First, at low current densities, activation overpotentials mainly causes the cell voltage increases. Second, between 0.1 and 0.4 A cm^{-12} the polarisation curve is nearly linear. Finally, strongly increasing ionic voltage losses, due to an insufficient water management, determine the scope of the polarisation curve up to the limiting current density.

Thin membranes.—A mitigation strategy against the previously discussed membrane dehydration and the corresponding high cell

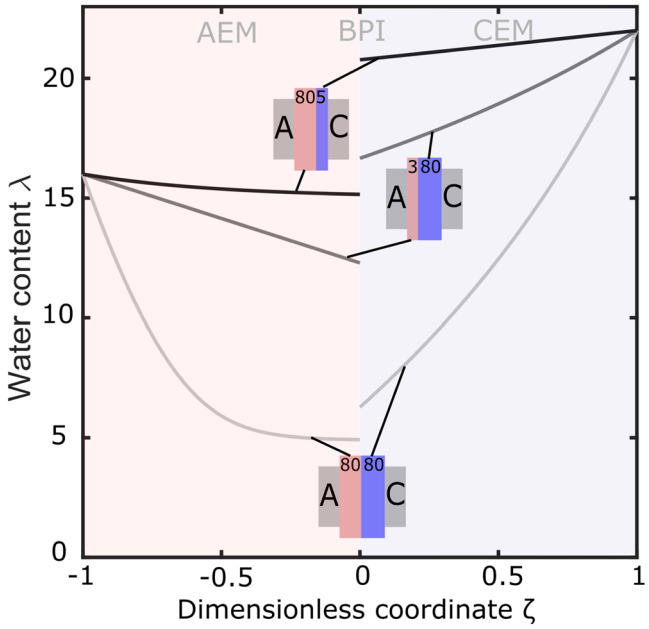

Figure 7. Comparison of decreased membrane thicknesses and the impact of increased water content, the effect is higher with a decreased CEM thickness. Conditions: p = 1 bar, T = 80 °C and i = 0.5 A cm^{-2}.

voltages is discussed in this section. For this purpose, the above-discussed base case with two equally thick membranes (80 μm each) is extended by two extreme configurations. In these configurations, the membrane thickness of either the AEM or the CEM is decreased to 3 μm because of better comparison with the experimental results of Mayerhöfer et al.[6] and 5 μm, respectively, while the other membrane remains 80 μm thick.

In Fig. 7 the water content in the membranes is plotted over a dimensionless ζ-coordinate at a fixed current density of 0.5 A cm^{-2}. This dimensionless coordinate helps comparing the three cases, as the membrane thicknesses differ. Compared to the base case, using a *thin AEM* already shows higher water contents within the whole BPM. Using a *thin CEM* increases water content even more, only a small decrease appears between the water-saturated outer BPM boundaries and the BPI. In both cases with thin membranes (*thin AEM* and *thin CEM)* the reason for the higher water contents lies in the shorter diffusion path for the water and consequently improved diffusive water transport. Interestingly, by reducing the membrane thickness on one side, not only the water content of the corresponding side can be increased, but the other membrane side also benefits. Thus, in the case with the 5 μm thin CEM, it can be seen that the water content in the entire AEM (80 μm) is also higher and even higher than in the case with the 3 μm thick AEM.

In Fig. 8, the water fluxes to the BPI and the BPI water content is shown over the current density for the *Base Case*, the *thin AEM* and *thin CEM*. For better comparison with the other cases, the *Base Case* results from Fig. 5b are repeated in Fig. 8a.

The previously described positive effect on the increased diffusive transport due to reducing the membrane thickness can be seen very well for the case of the thin AEM, which is shown in Fig. 8b. Higher diffusive fluxes within the *thin AEM* feed the BPI and lead to an increased operating range compared to the *Base Case*. Whereas the total water supply across the AEM is negative in the *Base Case*, positive total water supply of the AEM to the BPI enables the cell to operate up to 2.35 A cm^{-2}. Before reaching the limiting current density, the water content gradient decreases inside the AEM and leads to a slight AEM diffusion decrease. On the CEM side, diffusion and drag flux are almost equal for low current densities. At higher current densities, the water transport by diffusion can be higher than by drag when water content is low

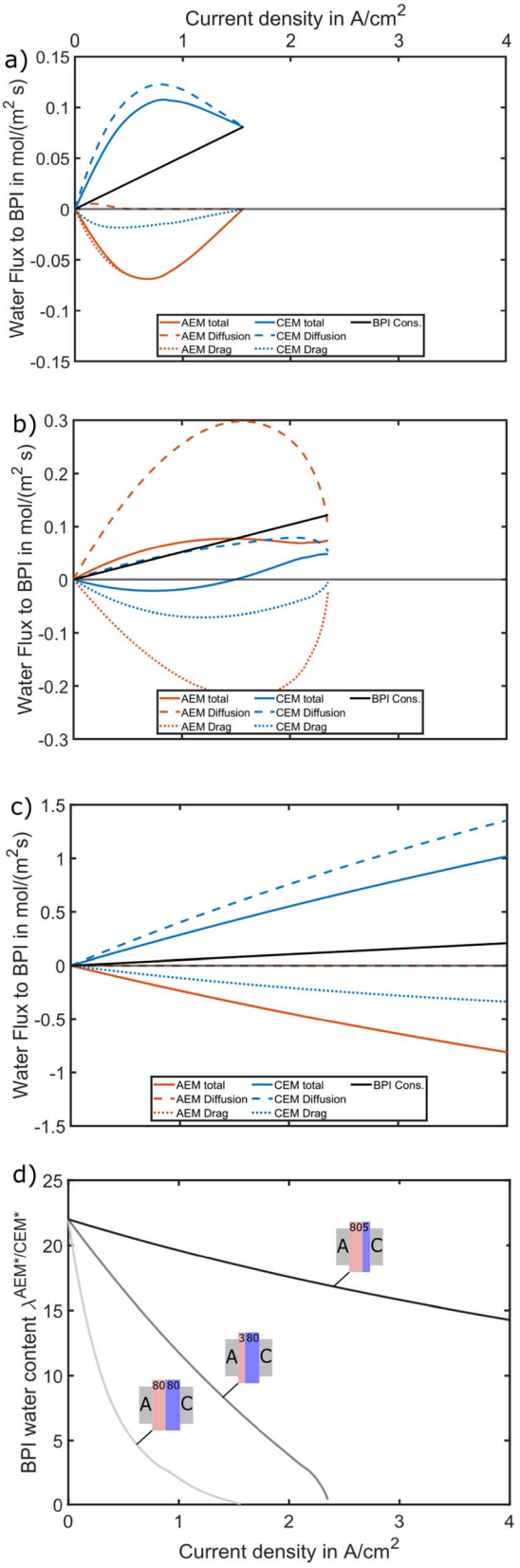

Figure 8. (a) Flux to BPI in Base Case with $\delta^{AEM} = \delta^{CEM} = 80$ μm. (b) Increased AEM diffusion and increased operating range due to thin AEM with $\delta^{AEM} = 3$ μm. (c) Decreased CEM thickness with $\delta^{CEM} = 5$ μm enables high current densities due to very high CEM water diffusion fluxes towards the BPI. d) BPI water content is increased with decreased membrane thicknesses compared to Base Case. Especially with a thin CEM, sufficient water is supplied to the BPI. Conditions: p = 1 bar, T = 80 °C.

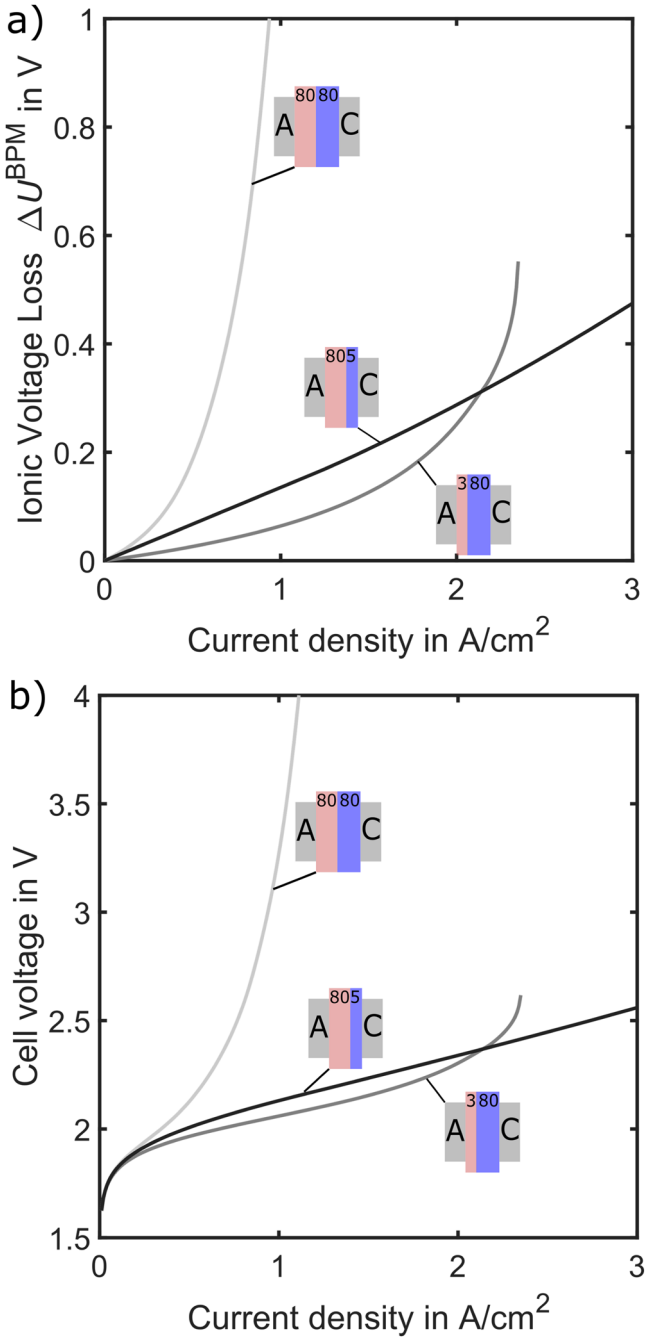

Figure 9. (a) Ionic BPM losses are reduced with decreased membrane thickness. At low until moderate current densities, the thin AEM case has the lowest ionic voltage losses. At higher current densities the BPM with the thin AEM starts to dry out, which cause an drastic increase in the voltage losses. Whereas, the case with the thin CEM has a very good water management, so that the ionic losses are almost linear. (b) Consequently, the polarisation curves for the thin membrane cases lie below the Base Case and the thin AEM case is favorable over the thin CEM case at low to moderate current densities until both curves intersect. Conditions: p = 1 bar, T = 80 °C.

close to the BPI. This can occur although the much thicker CEM compared to the AEM.

The diffusional flux through the CEM is enhanced even more with a *thin CEM*. This high diffusional flux feeds the high AEM drag, the CEM drag and the water splitting reaction, while diffusion through the AEM is negligibly small. A large operating range is enabled; the limiting current density is above 4 A cm^{-2}, as it can be seen as well in Fig. 8c.

In the *thin CEM* case, water content is still relatively high at 4 A cm^{-2} and a sufficient water transport is available, as it can be seen in Fig. 8c. The water content decreases almost linearly until 3 A cm^{-2}. A similar curve form exists for the *thin AEM* case over most current densities, however with a much stronger slope. Only short before the limiting current density, water content drops more sharply.

The water content effects the ionic voltage losses in the BPM, as shown in Fig. 9a. In the *thin CEM* case, an almost linear loss increase with current density arises, because the membrane resistance is almost constant. This is due to high water content within the BPM. AEM and CEM are wet and therefore conducive throughout the shown operating range. In the *thin AEM* case, the BPM dries out already at lower current densities. A concave ionic voltage loss increase appears inside the BPM in this case. Despite the faster dehydration in the thin AEM case, ionic voltage losses are lower up to 2.14 A cm^{-2} because of a generally more conductive CEM than AEM at high water content. Reducing the AEM thickness significantly decreases the ionic losses due to lower AEM than CEM conductivity. In terms of polarisation losses, a *thin AEM* is therefore favourable. Beyond the intersection of the *thin AEM* and *thin CEM* curve at 2.14 A cm^{-2}, the water content decrease of both membranes dominates the conductivity and consequently leads to higher ionic losses in the BPM for the *thin AEM* case, for which the water transport is the limiting factor. Above 2.14 A cm^{-2}, the counter-intuitive behaviour of the better polarization of the thin CEM is due to the good hydration of the BPM, since the well-hydrated BPM with a thick AEM is more ionically conductive than a dry BPM with a thick CEM.

These ionic voltage losses reflect in the polarisation curves as well (Fig. 9b). Generally, the polarisation curves of the *thin AEM* and the *thin CEM* are both below the *Base Case* curve, as also observed in previous experimental studies.[6,7] As expected from the ionic voltage losses shown in Fig. 9a, the *thin AEM* and the *thin CEM* polarisation curves intersect at 2.14 A cm^{-2} in Fig. 8b. Below 2.14 A cm^{-2}, the *thin AEM* configuration is preferable in terms of the polarisation curve to the *thin CEM* configuration. Only at high current densities, the *thin CEM* is favourable, because of the better water transport, which leads to higher water contents and an increased limiting current density. Generally, the setups with thin membranes are superior to the *Base Case* setup in both, polarisation and operating range.

Varying the membrane thickness.—A wider range of both membrane thicknesses from 80 μm to 2 μm is analysed in the following. At most AEM thicknesses, the CEM thickness determines the limiting current density (horizontal contours in Fig. 10a). The reason is the water content plateau at high current densities in these cases (cf. Fig. 5a. Consequently, diffusion through the CEM mainly drives water transport towards the BPI. Only at very low AEM thicknesses (approx. 10% of CEM thickness), the AEM thickness affects the limiting current density. In these cases, water diffuses towards the BPI both, from the AEM and the CEM, as it was exemplarily shown before. Membrane thickness combinations within the white triangle would be smaller than 20 μm thick and are therefore assumed as too thin for real operation.

Beside the limiting current density, the voltage losses of the BPM become decisive in choosing the best thickness configuration. Figure 10b shows these ionic voltage losses of the whole BPM at a fixed current density of 0.5 A cm^{-2}. Both, a reduced AEM thickness and a reduced CEM thickness improves the performance and reduces the ionic voltage losses significantly. Reducing the AEM thickness reduces the voltage losses more than reducing the CEM thickness, due to the lower ionic conductivity of the AEM material. This can be seen in the slope of the lines with the similar BPM voltage losses. However, at higher total membrane thicknesses this effect is vanishing because of decreasing water transport and stronger effects of the dehydration on the ionic losses. In practical applications, a reduced AEM thickness is more favourable over a

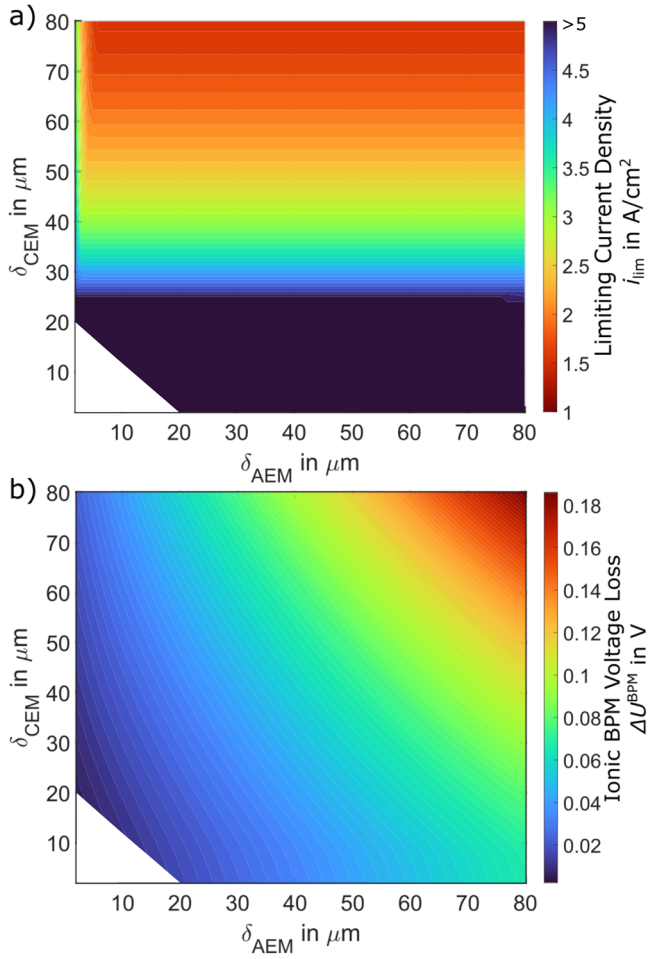

Figure 10. For safety reasons, membrane thickness combinations within the white triangle are assumed as too thin for operation. (a) The limiting current density is mainly determined by the CEM thickness. Only at very low AEM thicknesses (<10% of CEM thickness) lead the increased diffusion through the AEM to increases i_{lim}. (b) Ionic BPM voltage losses depend on both, AEM and CEM thickness. It is shown that the reduction of AEM thickness is even more advantageous for reducing voltage losses. In most practical solutions, lower cell voltages and therefore reduced AEM thicknesses are more favorable. Conditions: p = 1 bar, T = 80 °C and i = 0.5 A cm^{-2}.

reduced CEM thickness, due to the higher importance of electrochemical efficiency rather a wide operating range.

Conclusions

A 1D water transport model for the bipolar membrane water electrolysis (BPMWE) has been implemented and evaluated aiming to understand effects of decreasing membrane thicknesses. Effects of dehydration inside the BPM are considered in an electrochemical polarization model of the cell. Local effects of pH-gradients and implications for water transport and degradation are neglected in this model and leave a gap for further research.

At high current densities, the BPI dries out due a misbalance of water diffusion towards the BPI and water consumption of the water splitting reaction as well as electro-osmotic drag in AEM and CEM. In a setup with an equally thick AEM and CEM, water diffusion towards the BPI is higher through the CEM than through the AEM. The dehydration affects the polarization curve due to the strong dependence of the ionic conductivity of the BPM on water content. In particular, the low conductivity and the steeper dehydration of the AEM cause increases of the ionic BPM voltage losses. This emphasizes the importance of developing appropriate dehydration mitigation strategies in order to reach wider operating range and lower cell voltages for practical applications.

Using setups with decreased membrane thicknesses achieves higher limiting current densities. The operating range is sensitive especially to the CEM thickness. Decreasing the AEM thickness has an effect only with very thin AEMs. As the ionic conductivity is lower in the AEM, the BPM voltage losses are more sensitive to the AEM thickness. This means, there is a tradeoff between a wider operating range, which is mainly affected by the CEM thickness and the ionic losses of the BPM, where the AEM contributes more. We conclude that a decreased AEM thickness is more favorable, because of the lower ionic BPM losses and a higher importance of the cell efficiency rather than a wider operating range. However, for future development, the thicker CEM should also be as thin as possible to achieve a good operating range, but more importantly to further reduce the ionic losses.

Acknowledgments

We thank Ricarda Weiland for her comments, which greatly improved the quality of the manuscript in the final stages of writing. In addition, we gratefully acknowledge the financial support by the Federal Ministry of Education and Research in the framework of ReveAl (project number 03SF0662A).

Appendix

Reactions in Fig. 1.—Different setups are theoretically possible with BPM fuel cells and electrolysers. The reaction of these setups (cf. Fig. 1) are hereby listed:

Diffusion coefficients.—Diffusion coefficients for AEM and CEM are given by Peng et al.[13] and Wu et al.[21] respectively.

$$D^{\mathrm{AEM}} = 0.106063 \cdot 10^{-10} \cdot \lambda^{\mathrm{AEM}}$$

$$D^{\mathrm{CEM}} = 4.1 \cdot 10^{-10} \cdot \left(\frac{\lambda^{\mathrm{CEM}}}{25}\right)^{0.15} \cdot \left(1 + \tanh\left(\frac{\lambda^{\mathrm{CEM}} - 2.5}{1.4}\right)\right)$$

As uncertainty about the exact value and functionality of the AEM diffusion coefficients[22,23] and CEM diffusion coefficients[24–26] remains, the impact of the variation of the coefficients in a valuable range is shown in Table A·II.

Drag coefficients.—The AEM drag coefficient is fitted with data from Lu et al.[27] Beside this publication, only Li et al.[28] published measurements for the electro-osmotic drag coefficient in an area of $\lambda^{\mathrm{AEM}} > 15$, which showed coefficients in the same order of

Table A·I. Reactions in possible BPM fuel cell and electrolysis configurations.

	Acidic	Alkaline
HER	$2H^+ + 2e^- \longrightarrow H_2$	$4H_2O + 4e^- \longrightarrow 2H_2 + 4OH^-$
HOR	$H_2 \longrightarrow 2H^+ + 2e^-$	$2H_2 + 4\,OH^- \longrightarrow 4H_2O + 4e^-$
OER	$2H_2O \longrightarrow 4H^+ + 4e^- + O_2$	$4OH^- \longrightarrow O_2 + 2H_2O + 4e^-$
ORR	$4H^+ + 4e^- + O_2 \longrightarrow 2H_2O$	$O_2 + 2H_2O + 4e^- \longrightarrow 4OH^-$

Table A·II. Sensitivity of transport coefficients on limiting current density.

Coefficient variation	Limiting current density
No variation	1.56 A cm^{-2}
$D^{AEM} \cdot 2$	1.56 A cm^{-2}
$D^{AEM} \cdot 0.5$	1.56 A cm^{-2}
$D^{CEM} \cdot 2$	3.12 A cm^{-2}
$D^{CEM} \cdot 0.5$	0.78 A cm^{-2}
$n^{drag,\,AEM} \cdot 2$	1.56 A cm^{-2}
$n^{drag,\,AEM} \cdot 0.5$	1.55 A cm^{-2}
$n^{drag,\,CEM} \cdot 1.90$	1.10 A cm^{-2}

Table A·III. Additional equations and values for water splitting overpotential approach.

Parameter	Calculation/Value
Exchange current density	$i_{0,ws} = dFK_w k_f \cdot \exp\left(\frac{(1-\alpha_{ws})F\eta_{ws}}{RT}\right)$
Thickness space charge region	$d = \sqrt{\frac{2\varphi_{junc}\varepsilon_0\varepsilon_r}{qN_s}}$
—	$N_s = \frac{N_p N_a}{N_p + N_a}$
Junction potential	$\varphi_{junc} = \varphi_{eq} - \eta_{ws}$
Equilibrium junction potential	$\varphi_{eq} = 0.83$ V
Charge transfer coefficient	$\alpha_{ws} = 0.5$
Ion-product constant for water	$K_w = \exp\left(\frac{-79.89}{RT}\right) \cdot 10^{-14}$
Forward water splitting reaction constant	$k_f = 8 \cdot 10^{15}$
Vaccuum permittivity	$\varepsilon_0 = 8.85 \cdot 10^{-14} \frac{As}{Vm}$
Relative permittivity	$\varepsilon_r = 35$
Elementary charge	$q = 1.6 \cdot 10^{-19}$ C
Fixed charge density CEM	$N_p = 8.94 \cdot 10^{20}$ cm^{-3}
Fixed charge density AEM	$N_a = 1.32 \cdot 10^{21}$ cm^{-3}

magnitude. A wider data basis and further validating measurements would be advantageous. A variation of the coefficient is shown in Table A·II.

$$n^{drag,AEM} = -2.484 + 2.467 \cdot \ln(\lambda^{AEM} + 2.727)$$

CEM drag increases linearly with water content.[29]

$$n^{drag,CEM} = 2.5 \cdot \frac{\lambda^{CEM}}{22}$$

Higher drag coefficients are published up to 4.76 by Schalenbach et al.[30] at saturation ($\lambda^{CEM} = 22$), while more publications refer to a maximum drag coefficient of 2.5 at saturation.[21,24] The influence on the limiting current density is shown in Table A·II.

Absorption isotherms.—At the BPI, the activities of the two membranes are coupled. For the AEM, the activity-water content curve is fitted with data from Duan et al.[31] and $\lambda_{sat}^{AEM} = 16$.

$$\lambda^{AEM} = 42.98 \cdot a^3 - 43.19 \cdot a^2 + 16.35 \cdot a - 0.138$$

Similarly, activity and water content are fitted for the CEM side with data from Zawodzinski et al.[32] and $\lambda_{sat}^{CEM} = 22$.

$$\lambda^{CEM} = 64.38 \cdot a^3 - 65.98 \cdot a^2 + 23.75 \cdot a - 0.15$$

Ionic conductivities.—The ionic conductivity of the AEM is calculated with the curve of Peng et al.[13] and an Arrhenius-approach.[17,29]

$$\sigma_{52\,^\circ C}^{AEM} = 4.2 \cdot \frac{\lambda^{AEM}}{14};\ \lambda^{AEM} \leqslant 14$$

$$\sigma_{52\,^\circ C}^{AEM} = 4.2;\ \lambda^{AEM} > 14$$

$$\sigma^{AEM} = \sigma_{52\,^\circ C}^{AEM} \cdot \exp\left(\frac{11190}{R} \cdot \left(\frac{1}{325} - \frac{1}{T}\right)\right)$$

CEM-conductivity is calculated similarly.[29]

$$\sigma_{30\,^\circ C}^{CEM} = 0.5139 \cdot \lambda^{CEM} - 0.326$$

$$\sigma^{CEM} = \sigma_{30\,^\circ C}^{CEM} \cdot \exp\left(\frac{10543}{R} \cdot \left(\frac{1}{303} - \frac{1}{T}\right)\right)$$

Water splitting approach.—Additional values for calculation of the water splitting overpotential are given in Table A·III.[33]

ORCID

Oskar Weiland https://orcid.org/0000-0002-5135-1703

Patrick Trinke https://orcid.org/0000-0002-0935-5321
Boris Bensmann https://orcid.org/0000-0001-8685-7192
Richard Hanke-Rauschenbach https://orcid.org/0000-0002-1958-307X

References

1. S.-D. Li, C.-C. Wang, and C.-Y. Chen, *J. Membr. Sci.*, **330**, 334 (2009).
2. B. Huang et al., *JACS Au*, **1**, 1674 (2021).
3. L. Giordano, B. Han, M. Risch, W. T. Hong, R. R. Rao, K. A. Stoerzinger, and Y. Shao-Horn, *Catal. Today*, **262**, 2 (2016).
4. B. Yuzer, H. Selcuk, G. Chehade, M. E. Demir, and I. Dincer, *Energy*, **190**, 116420 (2020).
5. J. Xu, I. Amorim, Y. Li, J. Li, Z. Yu, B. Zhang, A. Araujo, N. Zhang, and L. Liu, *Carbon Energy*, **2**, 646 (2020).
6. B. Mayerhöfer, D. McLaughlin, T. Böhm, M. Hegelheimer, D. Seeberger, and S. Thiele, *ACS Appl. Energy Mater.*, **3**, 9635 (2020).
7. S. Z. Oener, L. P. Twight, G. A. Lindquist, and S. W. Boettcher, *ACS Energy Lett.*, **6**, 1 (2021).
8. Q. Li, J. Gong, S. Peng, S. Lu, P.-C. Sui, N. Djilali, and Y. Xiang, *J. Power Sources*, **307**, 358 (2016).
9. J. A. Wrubel, Y. Chen, Z. Ma, and T. G. Deutsch, *J. Electrochem. Soc.*, **167**, 114502 (2020).
10. H. Zhang, H. Wang, K. Jiao, and J. Xuan, *Appl. Energy*, **268**, 115053 (2020).
11. J. C. Bui, I. Digdaya, C. Xiang, A. T. Bell, and A. Z. Weber, *ACS Appl. Mater. Interfaces*, **12**, 52509 (2020).
12. A. Z. Weber, J. Newman, A. Z. Weber, and J. Newman, *J. Electrochem. Soc.*, **151**, A311 (2004).
13. S. Peng, X. Xu, S. Lu, P.-C. Sui, N. Djilali, and Y. Xiang, *J. Power Sources*, **299**, 273 (2015).
14. M. Carmo, D. L. Fritz, J. Mergel, and D. Stolten, *Int. J. Hydrogen Energy*, **38**, 4901 (2013).
15. R. García-Valverde, N. Espinosa, and A. Urbina, *Int. J. Hydrogen Energy*, **37**, 1927 (2012).
16. M. Hammoudi, C. Henao, K. Agbossou, Y. Dubé, and M. L. Doumbia, *Int. J. Hydrogen Energy*, **37**, 13895 (2012).
17. L. An, T. S. Zhao, Z. H. Chai, P. Tan, and L. Zeng, *Int. J. Hydrogen Energy*, **39**, 19869 (2014).
18. E. T. Ojong, J. T. H. Kwan, A. Nouri-Khorasani, A. Bonakdarpour, D. P. Wilkinson, and T. Smolinka, *Int. J. Hydrogen Energy*, **42**, 25831 (2017).
19. P. K. Giesbrecht, A. M. Müller, C. G. Read, S. Holdcroft, N. S. Lewis, and M. S. Freund, *Sustainable Energy Fuels*, **3**, 3611 (2019).
20. H. Hurwitz and R. Dibiani, *Electrochim. Acta*, **47**, 759 (2001).
21. H. Wu, P. Berg, and X. Li, *J. Power Sources*, **165**, 232 (2007).
22. T. D. Myles, A. M. Kiss, K. N. Grew, A. A. Peracchio, G. J. Nelson, and W. K. S. Chiu, *J. Electrochem. Soc.*, **158**, B790 (2011).
23. J.-P. Melchior and N. H. Jalarvo, *J. Phys. Chem. C*, **123**, 14195 (2019).
24. S. Dutta, S. Shimpalee, and J. W. van Zee, *Int. J. Heat Mass Transfer*, **44**, 2029 (2001).
25. K. Chadha, S. Martemianov, and A. Thomas, *Fuel Cells*, **21**, 139 (2021).
26. M. A. Raso, T. J. Leo, O. González-Espasandín, and E. Navarro, *Int. J. Hydrogen Energy*, **41**, 19766 (2016).
27. J. Lu, A. Barnett, and V. Molinero, *J. Phys. Chem. C*, **123**, 8717 (2019).
28. Y. S. Li, T. S. Zhao, and W. W. Yang, *Int. J. Hydrogen Energy*, **35**, 5656 (2010).
29. T. E. Springer, T. A. Zawodzinski, and S. Gottesfeld, *J. Electrochem. Soc.*, **138**, 2334 (1991).
30. M. Schalenbach, M. Carmo, D. L. Fritz, J. Mergel, and D. Stolten, *Int. J. Hydrogen Energy*, **38**, 14921 (2013).
31. Q. Duan, S. Ge, and C.-Y. Wang, *J. Power Sources*, **243**, 773 (2013).
32. T. A. Zawodzinski, C. Derouin, S. Radzinski, R. J. Sherman, V. T. Smith, T. E. Springer, and S. Gottesfeld, *J. Electrochem. Soc.*, **140**, 1041 (1993).
33. M. Ünlü, J. Zhou, and P. A. Kohl, *J. Phys. Chem. C*, **113**, 11416 (2009).